J. Iron Steel Res. Int. (2023) 30:305–316
https://doi.org/10.1007/s42243-022-00880-7

ORIGINAL PAPER

# Preparation of $Fe_3Si$ and FeSi intermetallic compounds from copper slag by electrochemical method

Hui Li[1] · Chao-long Xue[1] · Yu Yang[2] · Jing-long Liang[1]

Received: 5 January 2022 / Revised: 6 June 2022 / Accepted: 5 August 2022 / Published online: 22 December 2022


**Abstract**
$Fe_3Si$ and FeSi intermetallic compounds were prepared by $CaCl_2$–NaCl melt electrolysis at 800 °C from the non-magnetic copper slag compound. The phase transition of the cathode particles with different electrolysis voltages and durations was investigated by X-ray fluorescence spectroscopy, inductively coupled plasma spectroscopy, X-ray diffraction, and scanning electron microscopy. The results showed that $Fe_3Si$ and FeSi intermetallic compounds can be obtained by one-step electrolysis for 10 h at 3.2 V and two-step electrolysis of 2.5 V for 4 h and 3.2 V for 6 h. However, the current efficiency increased from 31.70% of one-step electrolysis to 39.87% of two-step electrolysis. The formation of $Fe_3Si$ and FeSi intermetallic compounds is a gradual evolution process with the increase in Si content, following the formation law of Fe → FeSi → $Fe_3Si$ + FeSi → FeSi. The metallic impurities of the final product were 1.29 wt.% Mg and 3.85 wt.% Al, respectively.

**Keywords** Ferroalloy · Intermetallic compound · Molten salt electrolysis · Copper slag · Formation process

## 1 Introduction

Ferroalloys (including ferrosilicon, ferromanganese, ferroaluminum, ferrotungsten, etc.) are essential raw materials in steelmaking process, used as steelmaking deoxidizers, alloy additives, and reducing agents for metal oxides [1–4]. More than 90% of ferroalloys are consumed in the steelmaking process. As one of the most important and productive ferroalloys, ferrosilicon has a wide range of applications in deoxidizers, reducing agents for metal oxides, additives for refractories, and electrode materials [5–7]. At present, the preparation of ferrosilicon alloy has attracted extensive attention. Brack et al. [8] synthesized activated ferrosilicon-based microcomposites by ball milling method, which showed excellent hydrogen generation performance. Aryanto and Sudiro [9] prepared ferrosilicon–aluminum coating using a mechanical alloying technique and carried out thermal annealing study on its structural characteristics, and the results show that the thickness of $Fe_3Al_2Si_3$ and Si-rich layer increased as annealing temperature increased. He et al. [10] prepared ferrosilicon alloy granules using a rotary multi-nozzles cup atomizer, and the prepared ferrosilicon granules meet the industrial requirements and show a good deoxidation effect. Xue et al. [11] developed a clean process for preparing alumina and ferrosilicon alloy by vacuum thermal reduction using fly ash as raw material and achieved good recovery effect. However, in the traditional preparation process of ferrosilicon with silica, steel, and coke as raw materials, ferrosilicon is obtained by electric furnace high-temperature (1500–1800 °C) reduction. Due to the use of silica and coke as raw materials, as well as the high reduction temperature, the process energy consumption and production cost were greatly increased [12]. In view of this issue, it is very important to explore low-cost raw materials and develop low-energy consumption preparation methods.

Copper slag is the by-product of copper refining process. About 50 million tons of copper slag is produced every year

✉ Jing-long Liang
ljl@ncst.edu.cn

[1] Key Laboratory of Ministry of Education for Modern Metallurgy Technology and College of Metallurgy and Energy, North China University of Science and Technology, Tangshan 063009, Hebei, China

[2] Comprehensive Testing and Analyzing Center, North China University of Science and Technology, Tangshan 063009, Hebei, China

in the world [13]. Because of its high contents of iron and silicon, copper slag has attracted extensive attention in recent years [14–16]. The main phase of copper slag is iron olivine, and the rest contains a small amount of magnetite and silicate [17]. The most valuable element extracted from copper slag by the current process is Fe, which makes it difficult to achieve high value-added utilization [18, 19]. However, the high contents of Fe and Si in copper slag make it possible to be used as raw material for preparing ferrosilicon. Therefore, it is necessary to explore a novel, effective, and green treatment process to achieve high recovery efficiency and high economic efficiency of copper slag.

In recent years, using metal sulfides, nonmetal semiconductor oxides, or mixtures of multiple oxides as raw materials, molten salt electrolysis technology has been successfully used to prepare simple metal or alloys and nonmetal semiconductor materials, such as Fe–Si [20], Ti–Ge [21], Mg–Al–La [22], and Ta [23]. At present, direct molten salt electrochemical reduction of natural minerals and waste residue to extract metals or alloys has been studied. Li et al. [24, 25] successfully prepared $TiAl_3$ alloy by direct electrolysis of the mixture of titanium-bearing blast furnace slag and $Al_2O_3$ with solid oxygen permeable membrane as the anode. At the same time, the composite materials $Ti_5Si_3$/TiC and $Ti_5Si_3$/$Ti_3SiC_2$ were successfully prepared by electrolysis with appropriate proportions of $TiO_2$ and C, thereby realizing the high value-added product synthesis from titanium-bearing blast furnace slag. Mohanty and Muduli [26] prepared Fe–Ni alloy with low chromium and titanium contents by molten salt electrolysis using $Na_2CO_3$ aqueous solution immersed red mud. Compared with the traditional process, the molten salt electrolysis process has the advantages of high metal recovery rate, high product purity, low emission, and no by-products. Because the main phase of fayalite in copper slag is composed of FeO and $SiO_2$, it is worth considering to prepare ferrosilicon directly by electrolysis.

In this work, ferrosilicon intermetallic compounds containing a small amount of Mg and Al are prepared by electrochemical reduction of copper slag in molten salt. In the electrochemical reduction process, the mechanism of the formation of ferrosilicon intermetallic compounds is studied and analyzed, and the electrolysis process is optimized to improve the current efficiency. Finally, the evolution process of the ferrosilicon intermetallic compound is determined.

## 2 Experimental

### 2.1 Raw material and precursor preparation

The copper removed tailings of the flash furnace copper smelting were selected as the raw materials. The copper slag was uniformly mixed with 10 wt.% absolute ethanol and subjected to mechanical ball milling for 5 h at 250 r/min with a ball-to-powder mass ratio of 10:1. Then, magnetic separation experiment was conducted for the copper slag at a current intensity of 0.8–1.6 A. An average of three repeated experiments was taken for each group of experimental data, and the magnetic copper slag (MCS) and non-magnetic copper slag (NMCS) was magnetically separated. MCS is a high-quality iron-rich resource, and NMCS will be used for the synthesis of ferrosilicon. A disk with a diameter of 15 mm and a thickness of 1.5 mm was obtained by die pressing 0.8 g NMCS at 12 MPa for 5 min. The disks were sintered at 800 °C for 5 h (heating rate was 5 °C $min^{-1}$) to obtain precursors for the electrolysis experiment, and high-purity Ar (99.99%) was used as the protective gas during the sintering process.

### 2.2 Electrochemical reduction process

The cathode precursors were wrapped with 37 μm aperture iron mesh and then fixed on the stainless steel rod with iron wire. The anode graphite sheets (purity > 99.99%, length of 100 mm, width of 15 mm, and height of 3 mm) were polished and washed repeatedly with deionized water and anhydrous ethanol; then, the graphite sheets were tied on the stainless steel rod. The prepared electrodes are shown in Fig. 1a. The $CaCl_2$–NaCl mixed salt ($CaCl_2$ and NaCl purity > 99.99%, and $CaCl_2$:NaCl = 1:1 in molar ratio) used as the electrolyte has the lowest eutectic point (504 °C), which make the electrolysis process to be carried out at low temperature [27]. The $CaCl_2$–NaCl mixed salt (180 g) placed in a corundum crucible was vacuum-dried at 250 °C for 24 h, and then, the mixed salt was programmatically heated to 800 °C in a resistance furnace. The pre-electrolysis experiment was conducted at 2.5 V to remove residual moisture and impurities in the molten salt [28]. Next, the electrolysis experiment was conducted at a voltage range of 1.2–3.2 V, with the electrolysis time varying from 1 to 15 h, the electrode spacing of 20 mm, and the high-purity Ar used as the protective gas throughout the experiment. The schematic diagram of electrolysis device is shown in Fig. 1b. After electrolysis, the cathode product was ultrasonically washed in deionized water to remove the molten salt in the sample and then vacuum-dried at 100 °C for 5 h.

### 2.3 Characterization

The chemical element compositions of the copper slag were analyzed by X-ray fluorescence spectroscopy (XRF-1800, Shimadzu Limited, Hong Kong, China) and inductively coupled plasma mass spectroscopy (ICP-MS, Agilent ICP-MS 7700, USA). The morphology and element

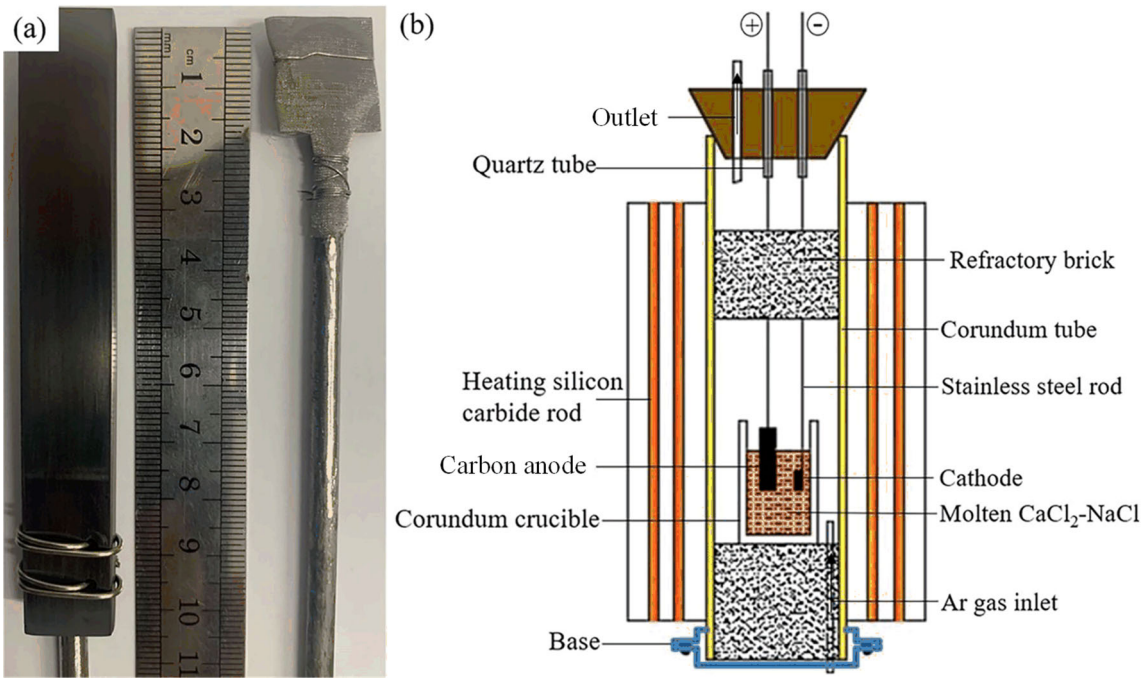


**Fig. 1** Photograph of graphite anode and copper slag compound cathode (**a**) and schematic diagram of molten salt electrolysis device (**b**)

composition of the cathodic products were examined by secondary and backscattered scanning electron microscopy (SEM, JSM-7900F, Japan) equipped with energy-dispersive X-ray spectroscopy (EDS) detector operating at 20 kV for imaging. The phase composition of the cathodic products was analyzed using an X-ray diffractometer (XRD, SmartLab SE, Japan) with Cu Kα radiation. Each scan was 5° to 90° and step size is 0.02°. X-ray photoelectron spectroscopy (XPS) was conducted on a Thermo Scientific$^{TM}$ K-Alpha$^{TM+}$ spectrometer equipped with a monochromatic Al Kα X-ray source (1486.6 eV) operating at 100 W. Samples were analyzed under vacuum ($< 10^{-6}$ Pa) with a pass energy of 150 eV (survey scans) or 50 eV (high-resolution scans). All peaks would be calibrated with C 1s peak binding energy at 284.8 eV for adventitious carbon.

## 3 Results and discussion

### 3.1 Raw materials of tailings of flash furnace copper smelting

The SEM images and the EDS analysis of the tailings are displayed in Fig. 2a–j. The EDS results show that the large particles at points 1 and 2 are mainly $Fe_3O_4$ and $Fe_2SiO_4$, respectively. According to the elemental analysis of point 3, a small part of Cu, S, and K exist in the fayalite ($Fe_2SiO_4$) phase and the magnetite ($Fe_3O_4$) phase, which do not appear in the XRD pattern because of the low content. The XRD results of the tailings of the flash furnace copper smelting are presented in Fig. 2k. The main phases are fayalite ($Fe_2SiO_4$) and magnetite ($Fe_3O_4$), and a broad band indicating the glass phase was observed between 10° and 40° in XRD patterns.

### 3.2 Effect of magnetic separation

The XRD patterns of the tailings before and after mechanical ball milling are presented in Fig. 3a. There is no phase change after ball milling, which indicated that no chemical reaction occurred in the milling process. The particle size analysis shown in Fig. 3b indicates that the average particle size of the tailings after ball milling for 5 h has dropped from 48.925 to 4.737 μm, and the fine particles are helpful to improve the deoxidation efficiency.

The mass of magnetic separation products versus magnetic separation current intensity curve is displayed in Fig. 4a. It can be seen that the recovery of MCS is low when the magnetic separation current intensity is 0.8 A. The reason may be that the attraction of a weak magnetic field on $Fe_3O_4$ is not very remarkable. With the increase in the current intensity, the recovery of MCS gradually increases and tends to a stable value. Yin et al. [29] found that increasing the magnetic field intensity will cause magnetic agglomeration of a small amount of NMCS. Therefore, high magnetic field intensity will make NMCS be attracted into MCS, resulting in the decline of Fe grade

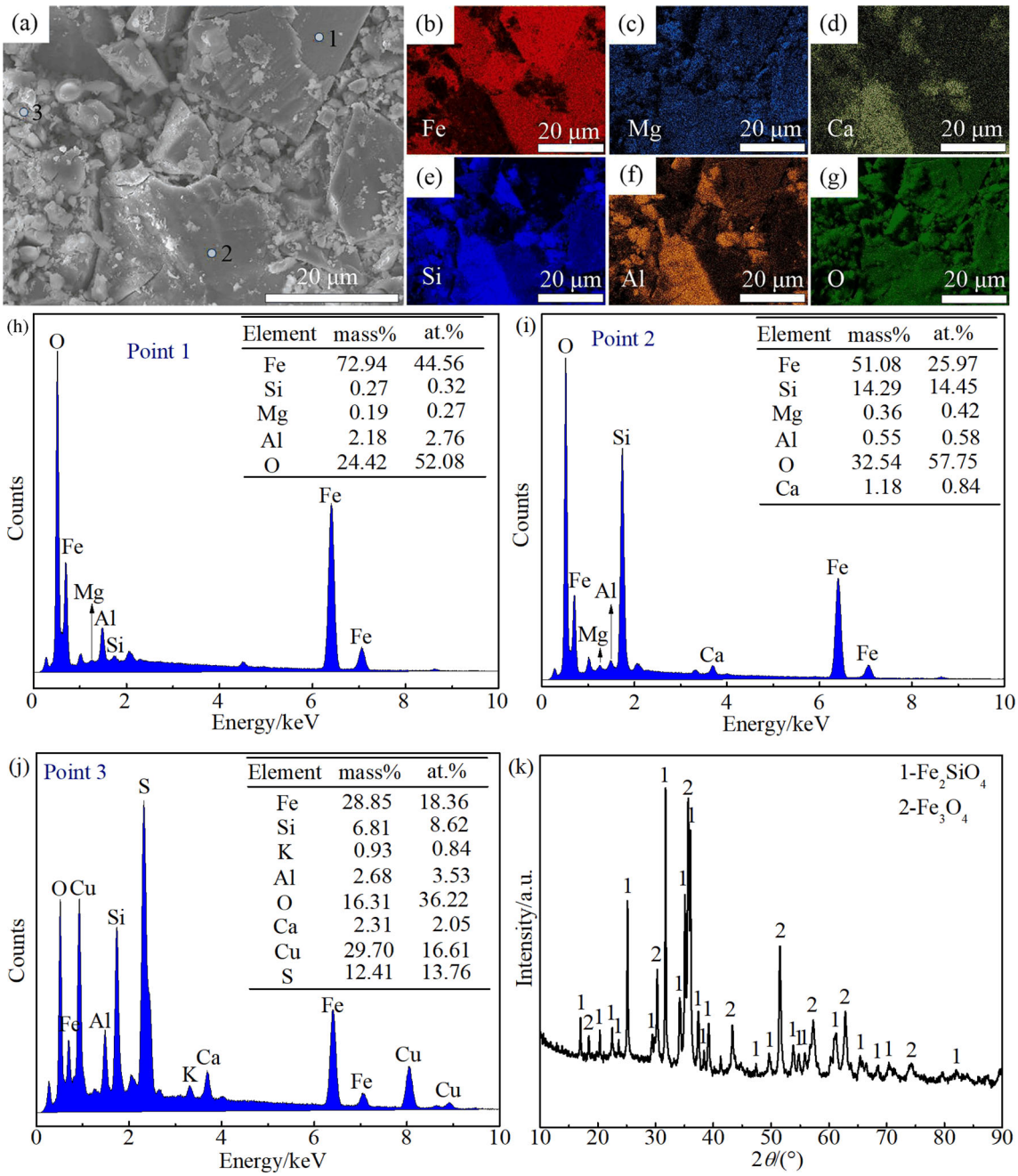


**Fig. 2** SEM image, EDS results and XRD pattern of copper slags. **a** SEM image; **b–g** EDS elemental mapping corresponding to SEM; **h** EDS of point 1 in **a**; **i** EDS of point 2 in **a**; **j** EDS of point 3 in **a**; **k** XRD pattern. $2\theta$—Diffraction angle

in MCS. Considering that a small amount of $Fe_3O_4$ can enhance the conductivity of the cathode precursors in the electrolysis process [30], which is helpful for the diffusion of the reduction reaction, the magnetic separation current intensity is selected as 1.2 A. The XRD patterns of NMCS and MCS at 1.2 A current intensity are shown in Fig. 4b. The main phase of NMCS is $Fe_2SiO_4$, and it also contains a small amount of $Fe_3O_4$ phase. The main chemical components and contents of the tailing and NMCS are shown in Table 1.

### 3.3 Influence of electrolysis voltage

The XRD patterns of cathode products electro-deoxidized at different voltages are shown in Fig. 5. The Fe phase appeared in the product at the voltage ranging from 1.2 to 1.4 V, which indicates that the actual reduction potential of

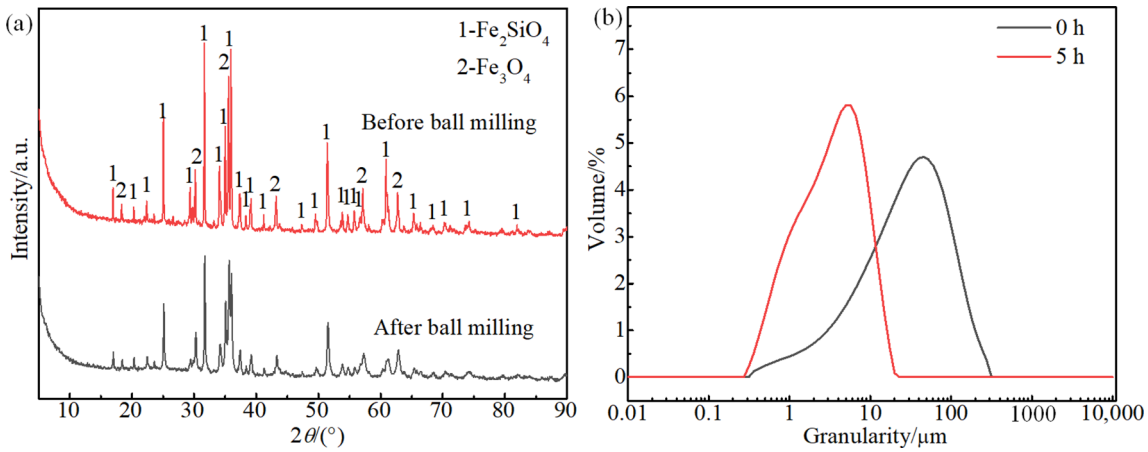


**Fig. 3** XRD patterns (**a**) and particle size analysis (**b**) of tailings before and after mechanical ball milling for 5 h

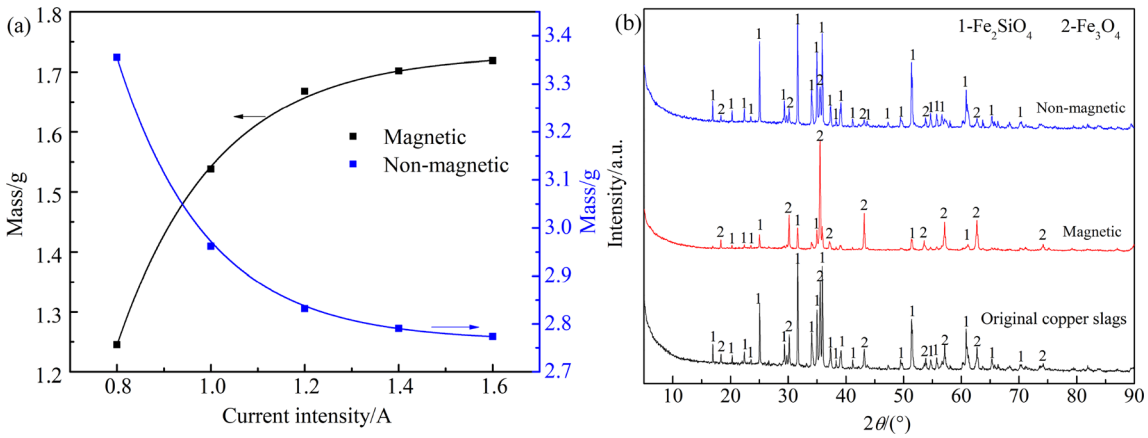


**Fig. 4** Mass of magnetic separation products versus magnetic separation current intensity curve (**a**) and XRD patterns of NMCS and MCS at magnetic separation current intensity of 1.2 A (**b**)

**Table 1** Chemical composition of tailings and NMCS (wt.%)

| Element | Fe | Si | O | Al | Ca | Zn | Mg | Cu | Others |
|---|---|---|---|---|---|---|---|---|---|
| Tailings | 32.84 | 17.92 | 39.83 | 4.22 | 1.34 | 1.48 | 0.85 | 0.25 | 1.27 |
| NMCS | 39.00 | 13.24 | 35.44 | 2.47 | 1.36 | 1.79 | 0.51 | 0.22 | 5.97 |

$Fe^{2+}$ and $Fe^{3+}$ has reached at this time, and the cathode reactions can be illuminated by reactions (1) and (2). $Cl^-$ and $Ca^{2+}$ in the molten salt penetrate the cathode sheet and combine with part of the oxide to form a complex silicate phase $Ca_8Mg(SiO_4)_4Cl_2$, $CaFeSiO_4$, and $Ca_3Fe_2(SiO_4)_3$ via reactions (3)–(5). These silicates nucleate and grow on the surface of the cathode, thereby hindering the diffusion and transfer of internal $O^{2-}$, resulting in a slower deoxidation process.

$$Fe_2SiO_4 + 4e = 2Fe + SiO_2 + 2O^{2-} \quad (1)$$

$$Fe_3O_4 + 8e = 3Fe + 4O^{2-} \quad (2)$$

$$8Ca^{2+} + 4Fe_2SiO_4 + MgO + 2Cl^- + 16e = Ca_8Mg(SiO_4)_4Cl_2 + 8Fe + O^{2-} \quad (3)$$

$$3Ca^{2+} + 3Fe_2SiO_4 + Fe_3O_4 + 14e = Ca_3Fe_2(SiO_4)_3 + 7Fe + 4O^{2-} \quad (4)$$

$$Ca^{2+} + Fe_2SiO_4 + 2e = Fe + CaFeSiO_4 \quad (5)$$

Rising the electrolysis voltage to 1.6–2.5 V, $CaFeSiO_4$ phase in the cathode product disappeared, which indicate that $Fe^{2+}$ was all reduced to Fe. The diffraction peak

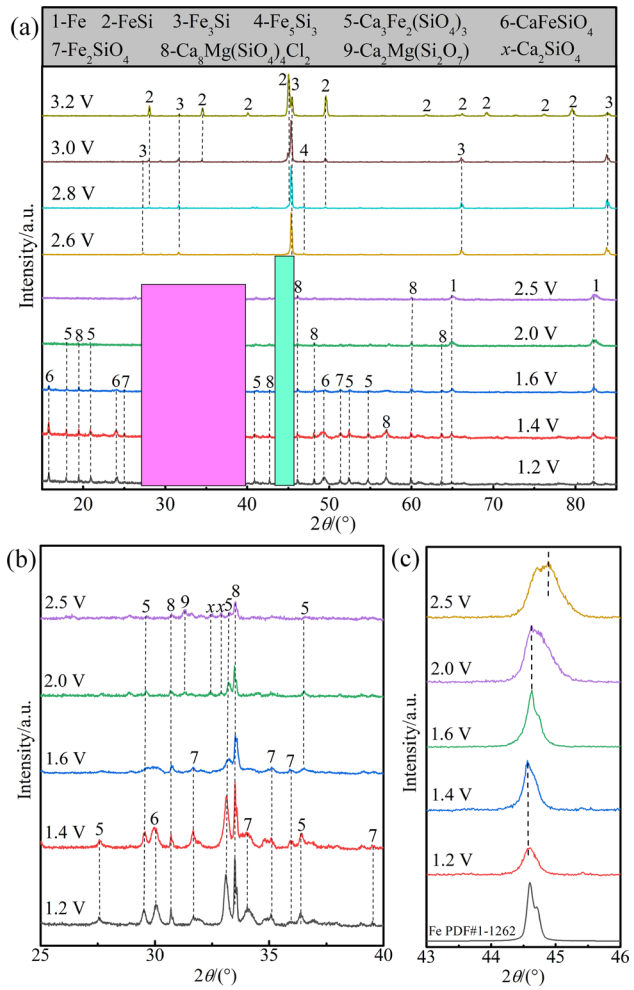


**Fig. 5** XRD pattern of cathode product with different electrolysis voltages at 800 °C for 10 h (**a**) and details of XRD (**b, c**)

intensities of $Ca_8Mg(SiO_4)_4Cl_2$ and $Ca_3Fe_2(SiO_4)_3$ decrease significantly with the increase in voltage. The SEM image and EDS analysis of the product of 2.5 V electrolysis for 10 h are presented in Fig. 6. The surface of the cathode sheet is loose and porous, and the particles are unevenly distributed. The elemental mapping result presented in Fig. 6b–e demonstrated that the elements of Fe and Si have the same element distribution. Combined with the XRD pattern in Fig. 5a, the large particles at points 1 and 2 have not been electrolyzed, and the fine particles at point 3 are mainly composed of Fe, Si, and Ca, indicating that $Si^{4+}$ has been partially electrochemically reduced. The reduced Si was solid-dissolved into the reduced Fe phase, which changed the crystal structure of Fe. Figure 5c clearly shows that the angle of the Fe(110) peak in the 1.6 V electrolysis product shifts to the right. This is because the atomic radius of Si is smaller than that of Fe, and the solid solution of Si in Fe changes the lattice constant of Fe [31]. According to the phase diagram of Fe–Si binary alloys calculated in the literature [32], the molar ratio of Si/(Si + Fe) is less than 0.123 in the α-Fe phase region, and the molar ratio of Si/(Si + Fe) in the product is 0.087, which is exactly in the α-Fe phase region.

Rising the electrolysis voltage to 2.6–3.2 V, $Ca_8Mg(SiO_4)_4Cl_2$ and $Ca_3Fe_2(SiO_4)_3$ disappeared, which demonstrates that $Si^{4+}$ was all reduced to Si, and furtherly, formed Fe–Si intermetallic compounds with the reduced metal Fe. The XRD pattern shows that the 3.2 V electrolysis products were FeSi and $Fe_3Si$.

Electrolysis voltage is the driving force of the electrolysis reaction and is proportional to the reaction rate. The greater the voltage, the faster the reaction rate. When the electrolysis voltage exceeds the decomposition voltage of $Fe_2SiO_4$ and $Fe_3O_4$, elemental Fe is not only derived from $Fe_2SiO_4$ and $Fe_3O_4$ in the cathode, but also produced by electrolytic reduction of intermediate products $CaFeSiO_4$ and $Ca_3Fe_2(SiO_4)_3$. According to the possible reaction between CaO and $SiO_2$ in molten salt and its Gibbs free energy, the Gibbs free energy of the reaction is negative, which indicates that $Ca^{2+}$ and $Si^{4+}$ in molten calcium salt are easy to form silicates in the process of electrolysis. The presence of $Ca^{2+}$ will promote $Si^{4+}$ in the molten salt to chemically react more preferentially during the electrolysis process, thereby generating a more stable silicate. Obviously, only the external driving force meets the conditions for silicate reduction, that is, when the voltage is greater than 1.6 V, $Si^{4+}$ will be reduced to Si on the cathode. A small amount of Si will dissolve into the reduced Fe at the voltage ranging from 1.6 to 2.5 V without changing the crystal structure of Fe phase. When the voltage exceeds 2.6 V, the amount of reduced Si was sufficient to form FeSi and $Fe_3Si$ intermetallic compounds with Fe.

Figure 7 displays the graph of the time–current relationship at different electrolysis voltages for 10 h. The current efficiency $\eta$ was calculated by the following formula:

$$\eta = nzF \times Q^{-1} \tag{6}$$

where $Q$ is the quantity of electric charge during electrolysis, C; $F$ is the Faraday's constant, $F$ = 96,485 C/mol; $z$ is the number of transferred electrons; and $n$ is the amount of substance of the theoretical product, mol [22]. The current efficiency of electrolysis for 10 h under different voltage conditions is listed in Table 2. As the electrolysis voltage increases, the background current and the amount of charge consumed in the electrolysis process increase, and the current efficiency will gradually decrease.

### 3.4 Effect of electrolysis duration

The time–current curve of the electrolysis of NMCS at 3.2 V is displayed in Fig. 8. Firstly, the current

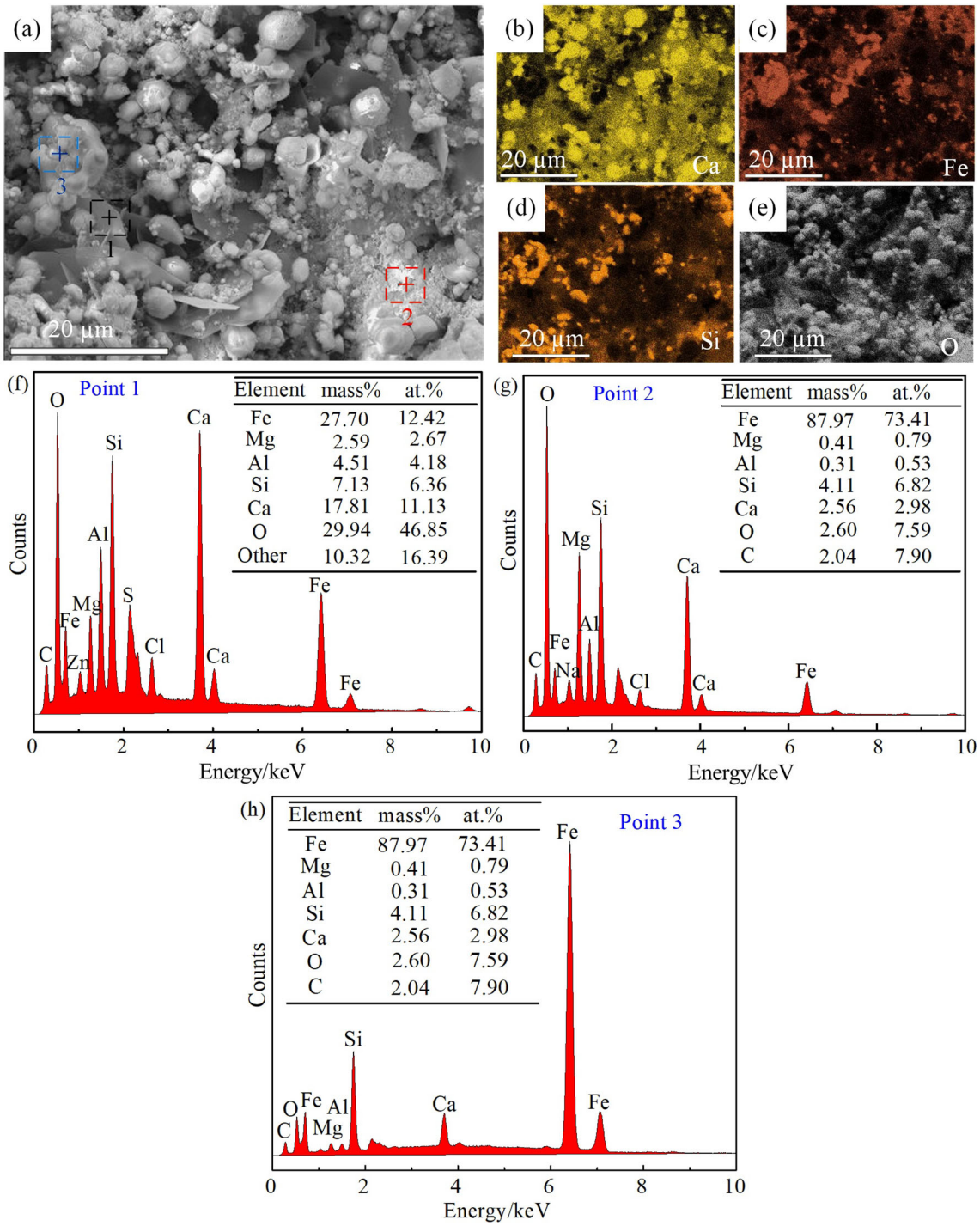


**Fig. 6** Product obtained by 2.5 V electrolysis for 10 h. **a** SEM image; **b–e** EDS elemental mapping corresponding to SEM; **f** EDS of point 1 in **a**; **g** EDS of point 2 in **a**; **h** EDS of point 3 in **a**

instantaneously rises to 2.54 A after electrolysis, which indicates the charging process of the electric double layer of the three-phase boundary (3PI) of the current collector (iron mesh)/metal oxide/electrolyte (molten salt) [33]. Then, the reduction starts at 3PI; the $O^{2-}$ at the interface is removed; $Fe^{2+}$ and $Fe^{3+}$ first get electrons and then are reduced; $O^{2-}$ migrates to the anode under the action of the electric field; and the current drops rapidly. Because the reduction voltage of $Si^{4+}$ was lower than 3.2 V, a small amount of $Si^{4+}$ is reduced after gaining electrons, and forms $Fe_3Si$ and FeSi intermetallic compounds with the reduced Fe after the reduction of $Fe^{2+}$ and $Fe^{3+}$ is

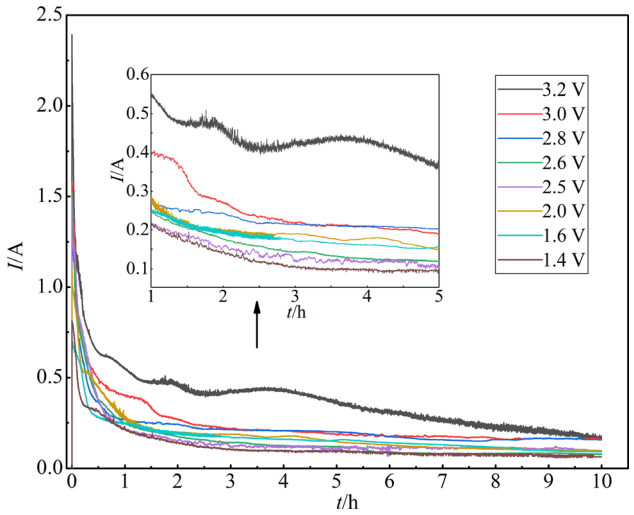


**Fig. 7** Time ($t$)–current ($I$) curve of 1.2–3.2 V electrolysis at 800 °C for 10 h

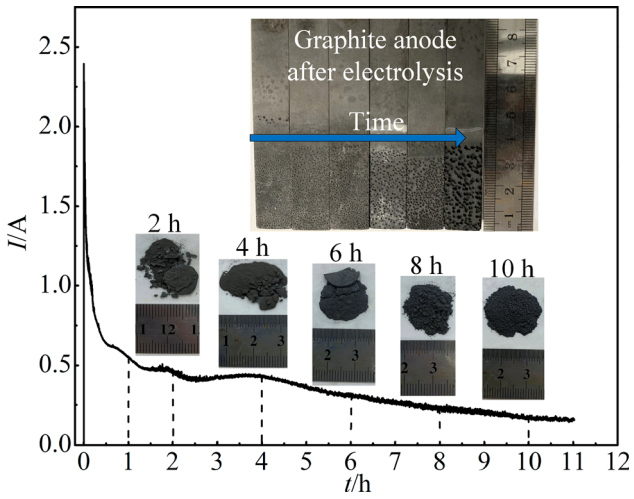


**Fig. 8** Time–current curve of NMCS compound electrolyzed at 3.2 V for 10 h

completed. When the reduction of 3PI is completed, the reduced Fe and Si as new conductors form new 3PI with unreduced compounds and molten salts, allowing the reaction to continue toward the interior of the cathode. The internal $O^{2-}$ needs to diffuse to the electrode/molten salt interface by solid diffusion in the cathode precursor. $O^{2-}$ removed from cathode precursor can react with $SiO_2$, $Na^+$, and $Ca^{2+}$ to form the complex compound $Na_2CaSiO_4$, which hinders the removal of $O^{2-}$ and decreases the reduction reaction rate. Obvious fluctuations appeared on the electrolysis curve. The electrolysis rate was relatively fast throughout the process, and the current dropped to 0.697 A within 1 h. During the electrolysis time ranging from 1 to 4 h, the peak intensity of Fe in the cathode reduction product gradually weakens, while the peak intensity of $Fe_3Si$ and FeSi slowly increases, and the $Na_2CaSiO_4$ peak does not change significantly; the electrolysis current tends to be stable.

**Table 2** Current efficiency of electrolysis for 10 h under different voltage conditions

| Voltage/V | Cathode mass/g | Theoretical charge/C | Actual charge/C | Current efficiency/% |
|---|---|---|---|---|
| 3.2 | 0.7699 | 4306.23 | 13,586.10 | 31.70 |
| 3.0 | 0.7602 | 4273.63 | 8781.43 | 48.67 |
| 2.8 | 0.7684 | 4300.91 | 7878.44 | 54.59 |
| 2.6 | 0.7693 | 4303.91 | 5598.30 | 76.88 |
| 2.5 | 0.7679 | 4299.25 | 5815.33 | 73.93 |
| 2.0 | 0.7639 | 4285.94 | 6539.68 | 65.64 |
| 1.6 | 0.7702 | 4306.90 | 6070.74 | 70.95 |
| 1.4 | 0.7721 | 4313.22 | 4390.06 | 98.25 |

XRD patterns of electrolysis products of NMCS compound at 3.2 V at different time are shown in Fig. 9. Further increasing the electrolysis time to 6–8 h, $Si^{4+}$ was gradually decreased, which was manifested as a small decrease in current. The peak intensity of $Na_2CaSiO_4$ decreases significantly, which indicate that $Na_2CaSiO_4$ was gradually separated and reduced to Si. The peak of Fe disappeared, which can be illuminated by the reactions between Si and Fe to transform into FeSi. $Na_2CaSiO_4$ phase was not found in the product of 10 h electrolysis, indicating that the reaction was complete. Due to the reaction between $O^{2-}$ accumulated near the electrode and $Ca^{2+}$ in the melts ($Ca^{2+} + O^{2-} = CaO$), CaO was produced in the electrolysis process. The appearance of $CaCO_3$ in the product was attributed to the C cycle in the electro-deoxidation process [34]. As the electrolysis time increases to 10 h, the final products are only FeSi and $Fe_3Si$, and the current drops to 0.2 A.

Increasing the electrolysis time, the larger particle size of the silicate was reduced, and the smaller particle size of the alloy phase was gradually formed, as shown in Fig. 10. After 10 h of electrolysis, the product contains a small amount of Al and Mg in addition to Fe and Si. The results of surface elements mapping are shown in Fig. 10b. The distribution of the elements of Fe, Si, Al, and Mg was overlapped, which indicate that Al and Mg were reduced and alloyed with Fe–Si intermetallic compound. The results show that the content of Mg and Al in cathode is 1.29 and 3.85 wt.%, respectively. The current efficiency of the whole process is only 31.70%. The reason for the low current efficiency is the by-product $CaCO_3$ produced in the electrolysis process, and the impurity C in the product is also attributed to the electrochemical reduction of $CaCO_3$ [35]. The use of inert anode can effectively avoid C

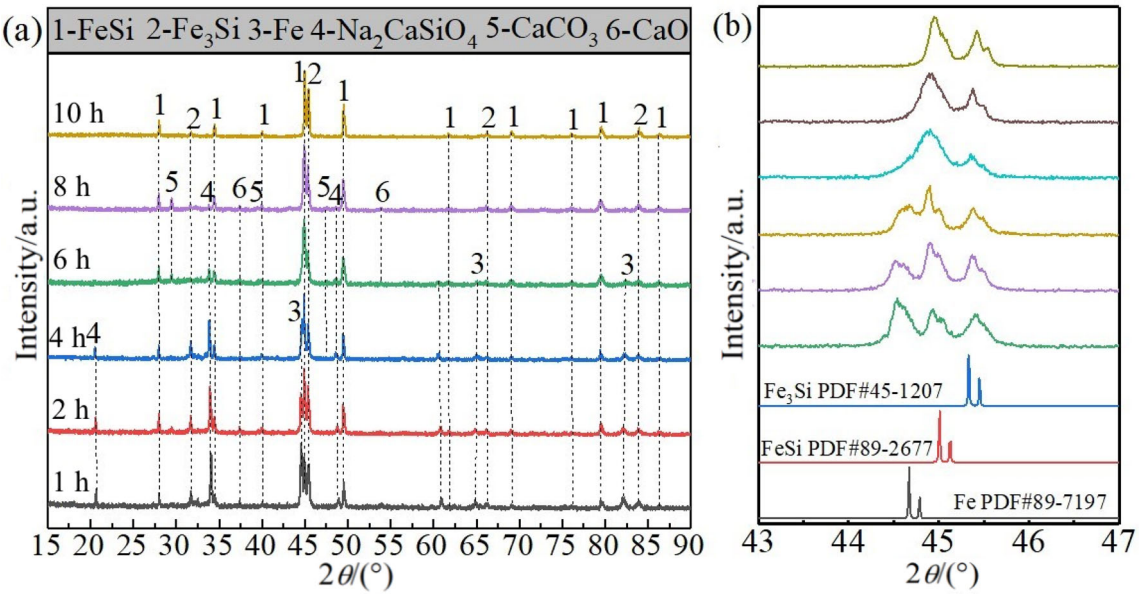


**Fig. 9** XRD pattern of electrolysis products of NMCS compound at 3.2 V at different time (**a**) and details of XRD patterns (**b**)

contamination [36]. The XPS of the product obtained after 10 h of electrolysis at 3.2 V is shown in Fig. 11. The results demonstrated that Fe and Si existed in the product, which means that the iron–silicon alloy was produced in the electrolysis process.

To improve current efficiency, a stepwise voltage change method was used in the electrolysis process. The time–current curve of the step electrolysis is displayed in Fig. 12a, in which 2.5 V electrolysis for 4 h is applied in the first stage, and 3.2 V electrolysis for 6 h is applied in the second stage. As shown in Fig. 12b, there is no $Fe_3Si$/FeSi alloy formation in the product after 4 h of 2.5 V electrolysis, and it is different from the product after 3.2 V electrolysis for 10 h. The reason is that the simultaneous reduction of Fe and Si under high voltage causes the uneven distribution of Fe and Si, which makes the reaction process unable to accurately follow α-Fe → $Fe_3Si$ → $Fe_3Si$/FeSi, but a one-step transformation of α-Fe → $Fe_3Si$/FeSi. Using segmented electrolysis, the later-reduced Si reacts preferentially with the excess of the first-reduced Fe to form $Fe_3Si$. After Fe gradually disappeared, the reduced Si will furtherly react with $Fe_3Si$ to form FeSi. Therefore, the $Fe_3Si$ content in the product with segmented electrolysis was significantly higher than FeSi, and the current efficiency of the whole process was increased from 8.71% to 39.87%.

## 3.5 Mechanism of FeSi/$Fe_3Si$ electrochemical synthesis

The electrochemical synthesis process of $Fe_3Si$ and FeSi can be divided into three parts: (1) the formation and reduction of Fe/Si containing oxides, (2) the formation and reduction of Si oxides, and (3) the evolution and formation of $Fe_3Si$ and FeSi phases. $Fe_3O_4$ and $Fe_2SiO_4$, the main substances in NMCS, were electrolyzed in $CaCl_2$–NaCl molten salt to generate $Fe_3Si$ and FeSi. The electrochemical reduction mechanism of this process was obtained. Since the Si–O tetrahedral structure was more stable than the octahedral structure, Fe in $Fe_2SiO_4$ will be reduced first in the electrolysis process. At the same time, the $Ca^{2+}$ and $Na^+$ in the molten salt were embedded in the cathode sheet and reacted with $SiO_2$ and $O^{2-}$ in the cathode to form $Na_2CaSiO_4$. As the electrolysis time increased, $Na_2CaSiO_4$ was electrolytically reduced to Si. Finally, the reduced Si and Fe form $Fe_3Si$ and FeSi, and as the Si content increases, $Fe_3Si$ will further react with Si to form FeSi, as shown in Fig. 13.

According to the Fe–Si binary phase diagram, the transformation sequence of the metal phase was α-Fe → $Fe_3Si$ → $Fe_3Si$/FeSi → FeSi at 800 °C. When the molar ratio of Si/(Si + Fe) was less than 0.123, a small amount of Si will not affect the existence of α-Fe, which can be demonstrated by XRD and SEM of the product of 1.6–2.5 V electrolysis for 10 h. As the molar ratio of Si/(Si + Fe) exceeds 0.123, the α-Fe phase gradually transformed into the $Fe_3Si$ phase. As the molar ratio of Si/(Si + Fe) exceeds 0.297, the $Fe_3Si$ phase is transformed into the coexistence zone of $Fe_3Si$ and FeSi, which is consistent with the phase formation sequence in the electrolysis process. Therefore, the formation of Fe–Si intermetallic compounds in the electrochemical reduction process was a gradual evolution process.

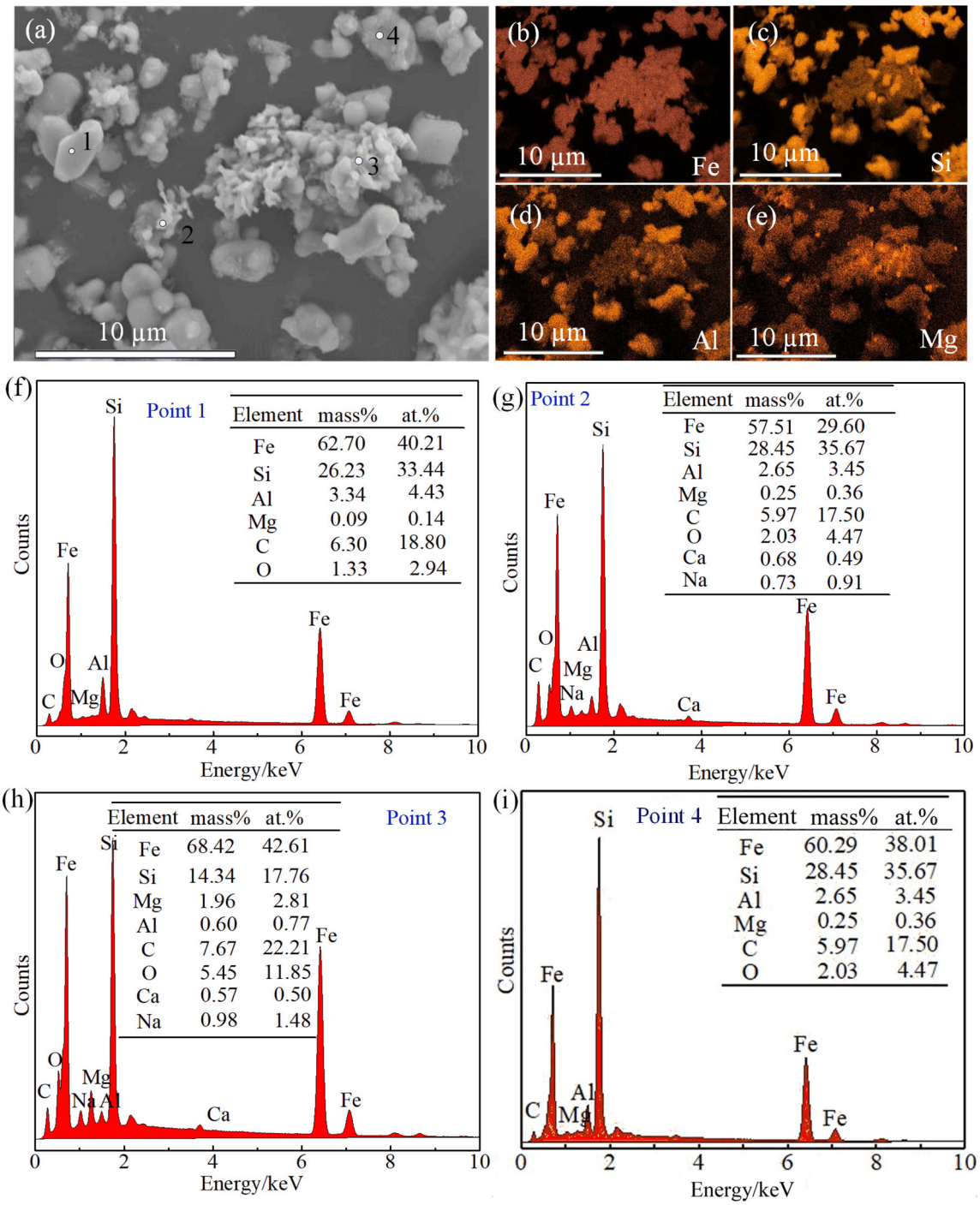


**Fig. 10** Product obtained after 10 h of electrolysis at 3.2 V. **a** SEM image; **b–e** EDS elemental mapping corresponding to SEM; **f** EDS of point 1 in **a**; **g** EDS of point 2 in **a**; **h** EDS of point 3 in **a**; **i** EDS of point 4 in **a**

## 4 Conclusions

$Fe_3Si$ and FeSi intermetallic compounds were synthesized by direct electrolysis of NMCS compound powders in molten $CaCl_2$–NaCl at 800 °C with a potential of 3.2 V. The reaction mechanism for the synthesis of $Fe_3Si$/FeSi includes three periods: the formation and reduction of iron oxide compounds, the formation and reduction of silicon oxide compounds, and the formation of $Fe_3Si$ intermetallic compound. The formation of $Fe_3Si$ and FeSi intermetallic compounds in the electrochemical reduction process was a gradual evolution process. A small amount of Al and Mg oxides/compounds contained in the copper slag is reduced to elemental substances and exists in $Fe_3Si$ and FeSi

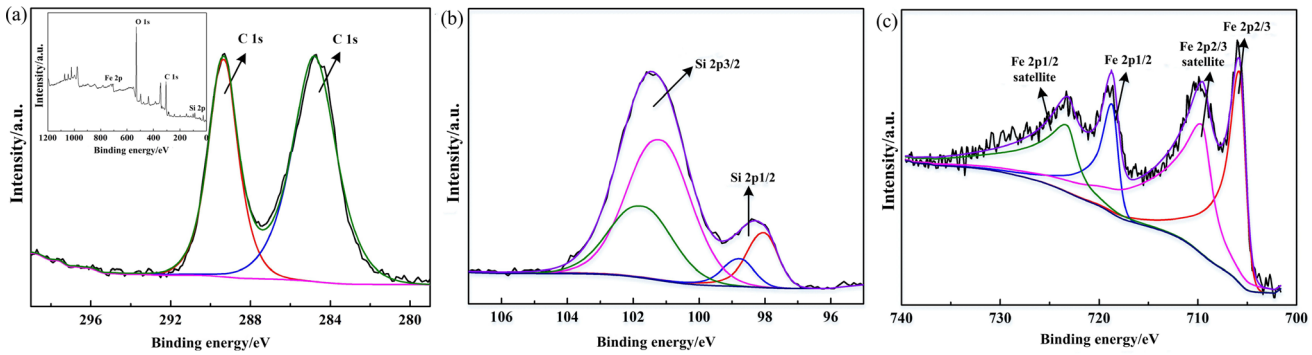


**Fig. 11** XPS of product obtained after 10 h of electrolysis at 3.2 V. **a** C 1s spectrum, inset showing XPS survey spectrum of product; **b** Si 2p spectrum; **c** Fe 2p spectrum

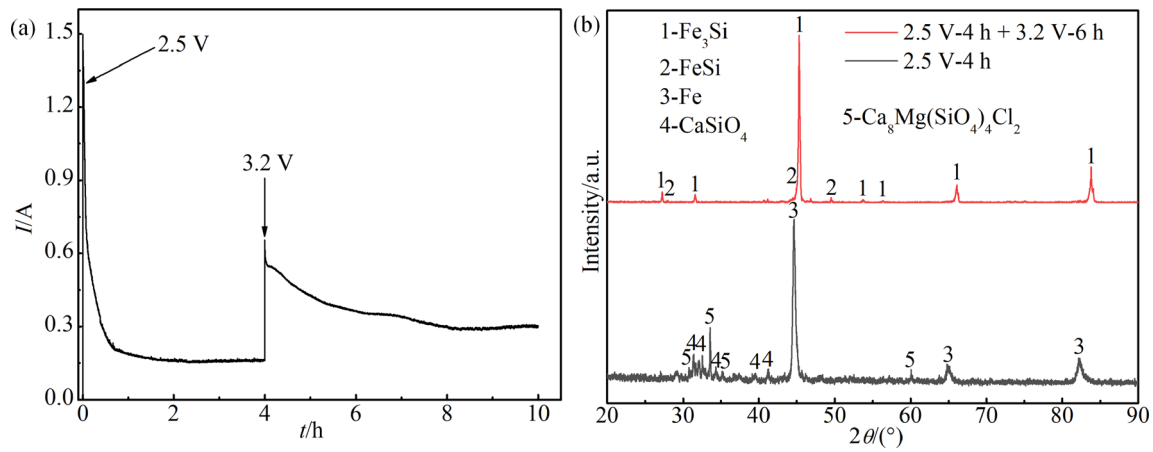


**Fig. 12** Time–current curve of step electrolysis (**a**) and XRD pattern of product by step electrolysis (**b**)

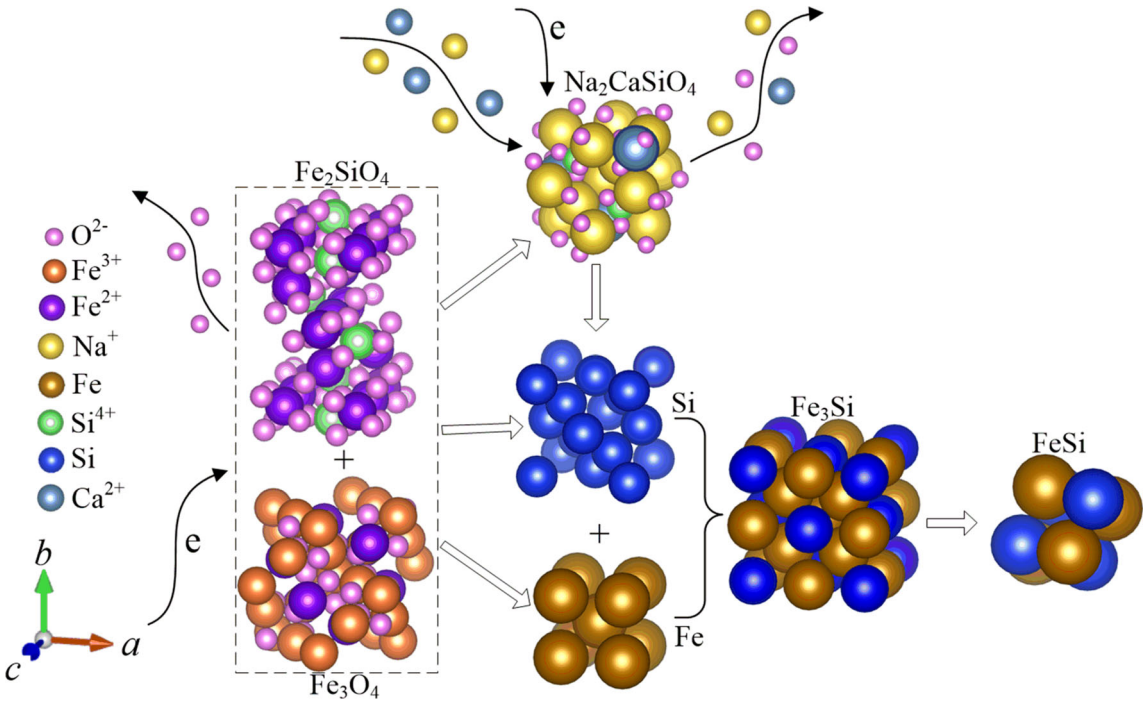


**Fig. 13** Schematic illustration of reaction mechanism of electrochemical deoxidation of NMCS compound precursor to $Fe_3Si$ intermetallic

intermetallic compound. To improve current efficiency, a stepwise voltage change method was used in the electrolysis process. The $Fe_3Si$ content in the product with segmented electrolysis was significantly higher than FeSi, and the current efficiency of the whole process was increased from 8.71% to 39.87%.

Overall, this study is based on the molten salt electrolysis process, which provides a method for the efficient recovery of valuable elements in copper slag. The research results and theoretical explanations will promote the research on the electrolytic extraction of valuable elements from complex ore-phase molten salts.

**Acknowledgements** This work was supported by the National Natural Science Foundation of China (No. 52174315).

## Declarations

**Conflict of interests** The authors declare that they have no known competing financial interests or personal relationships that could have appeared to influence the work reported in this paper.

## References

[1] G.K. Dalapati, C.C. Tan, S. Masudy-Panah, H.R. Tan, D. Chi, Mater. Lett. 159 (2015) 455–458.
[2] J. Safarian, ACS Sustainable Chem. Eng. 9 (2021) 5010–5026.
[3] M. Zamanzade, A. Barnoush, C. Motz, Crystals 6 (2016) 10.
[4] H.Y. Wang, Y. Hou, G.H. Zhang, K.C. Chou, ISIJ Int. 60 (2020) 636–639.
[5] W. He, H. Tian, S. Zhang, H. Ying, Z. Meng, W. Han, J. Power Sources 353 (2017) 270–276.
[6] E. Karamian, A. Monshi, S.M. Siadati, Mater. High Temp. 26 (2009) 357–363.
[7] J. Chen, N. Li, Y. Wei, B. Han, W. Yan, Ceram. Int. 42 (2016) 17650–17658.
[8] P. Brack, S.E. Dann, K.G.U. Wijayantha, P. Adcock, S. Foster, Int. J. Hydrogen Energy 44 (2019) 19113–19127.
[9] D. Aryanto, T. Sudiro, Surf. Coat. Technol. 337 (2018) 35–43.
[10] W. He, X. Lv, F. Pan, L. Gao, X. Li, J. Qiu, Adv. Powder Technol. 30 (2019) 895–902.
[11] Y. Xue, W. Yu, J. Mei, W. Jiang, X. Lv, J. Clean. Prod. 240 (2019) 118262.
[12] J.F. Wang, Y.H. He, Y. Jiang, H.Y. Gao, J.S. Yang, L. Gao, J. Wuhan Univ. Technol. Mater. Sci. Ed. 31 (2016) 242–247.
[13] X.Y. Wan, L.K. Hong, Y.H. Qi, J.J. Gao, Trans. Indian Inst. Met. 73 (2020) 2683–2691.
[14] P.G. Jiang, J.S. Liu, Y.Y. Xiao, X.H. Tan, W.J. Liu, J. Iron Steel Res. Int. 27 (2020) 796–806.
[15] C.D. Zhang, B. Hu, H.G. Wang, M.Y. Wang, X.W. Wang, Mining Metall. Explor. 37 (2020) 1241–1251.
[16] Y. Sharifi, I. Afshoon, S. Asad-Abadi, F. Aslani, J. Environ. Manage. 271 (2020) 111013.
[17] H.Q. Zhang, C.J. Hu, W.J. Gao, M.M. Lu, Minerals 10 (2020) 973.
[18] Q.J. Li, F.X. Yang, Z.Y. Wang, S.Y. Liu, Trans. Indian Inst. Met. 72 (2019) 3223–3231.
[19] S. Zhang, N. Zhu, F. Mao, J. Zhang, X. Huang, F. Li, X. Li, P. Wu, Z. Dang, J. Hazard. Mater. 402 (2021) 123791.
[20] K. Yasuda, T. Nohira, R. Hagiwara, Y.H. Ogata, Electrochim. Acta 53 (2007) 106–110.
[21] Y.S. Wang, X.L. Zou, X.G. Lu, S.S. Li, K. Zheng, S.J. Wang, Q. Xu, Z.F. Zhou, Trans. Nonferrous Met. Soc. China 28 (2018) 2351–2359.
[22] P.N. Jang, H.M. Li, W.J. Kim, S.C. Yun, G.H. Hwang, J. Mater. Res. Technol. 8 (2019) 5456–5463.
[23] R.P. Barnett, D.J. Fray, J. Mater. Sci. 49 (2014) 4148–4160.
[24] S.S. Li, X.L. Zou, K. Zheng, X.G. Lu, Q. Xu, C.Y. Chen, Z.F. Zhou, J. Alloy. Compd. 727 (2017) 1243–1252.
[25] S.S. Li, X.L. Zou, K. Zheng, X.G. Lu, C.Y. Chen, X. Li, Q. Xu, Z.F. Zhou, Metall. Mater. Trans. B 49 (2018) 790–802.
[26] J. Mohanty, R.C. Muduli, J. Inst. Eng. India Ser. C 101 (2020) 401–406.
[27] L. Xiong, Y.X. Hua, C.Y. Xu, J. Li, Y. Li, Q.B. Zhang, Z.R. Zhou, Y.D. Zhang, J.J. Ru, J. Alloy. Compd. 676 (2016) 383–389.
[28] Z.W. Liu, H.L. Zhang, L.L. Pei, Y.L. Shi, Z.H. Cai, H.B. Xu, Y. Zhang, Trans. Nonferrous Met. Soc. China 28 (2018) 376–384.
[29] W.Z. Yin, X.S. Yang, D.P. Zhou, Y.J. Li, Z.F. Lü, Trans. Nonferrous Met. Soc. China 21 (2011) 652–664.
[30] S. Franger, P. Berthet, J. Berthon, J. Solid State Electrochem. 8 (2004) 218–223.
[31] H.Q. Tang, J.T. Zhu, Z.Y. Tang, C.X. Ma, J. Electroanal. Chem. 731 (2014) 60–66.
[32] S.L. Cui, I.H. Jung, Calphad 56 (2017) 108–125.
[33] X.B. Jin, P. Gao, D.H. Wang, X.H. Hu, G.Z. Chen, Angew. Chem. 43 (2004) 733–736.
[34] G.Z. Chen, Int. J. Miner. Metall. Mater. 27 (2020) 1572–1587.
[35] X. Zou, X. Lu, Z. Zhou, C. Li, W. Ding, Electrochim. Acta 56 (2011) 8430–8437.
[36] Q. Huang, G. Zheng, T. Wu, Funct. Mater. Lett. 13 (2020) 2050032.